# Transition of Deformation Mechanisms in Single-Crystalline Metallic Nanowires

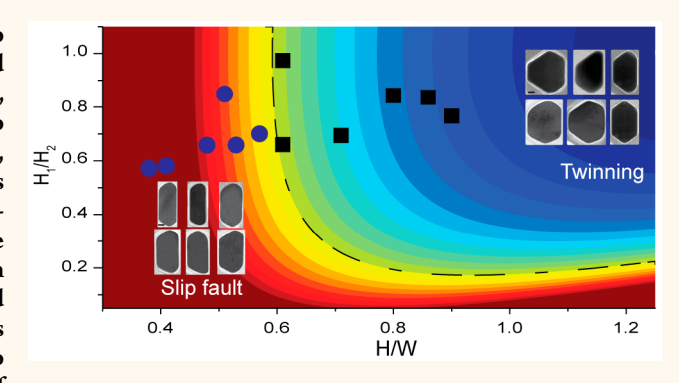
Sheng Yin, †,§,⊥6 Guangming Cheng,‡,⊥ Gunther Richter, Huajian Gao,\*,† and Yong Zhu\*,‡6

Supporting Information

see https://pubs.acs.org/sharingguidelines for options on how to legitimately share published articles.

Downloaded via BROWN UNIV on June 1, 2020 at 05:32:14 (UTC).

ABSTRACT: Twinning and dislocation slip are two competitive deformation mechanisms in face-centered cubic (FCC) metals. For FCC metallic nanowires (NWs), the competition between these mechanisms was found to depend on loading direction and material properties. Here, using in situ transmission electron microscopy tensile tests and molecular dynamics simulations, we report an additional factor, cross-sectional shape, that can affect the competition between the deformation mechanisms in single-crystalline FCC metallic NWs. For a truncated rhombic cross-section, the extent of truncation determines the competition. Specifically, a transition from twinning to localized dislocation slip occurs with increasing extent of



truncation. Theoretical and simulation results indicate that the energy barriers for twinning and dislocation slip depend on the cross-sectional shape of the NW. The energy barrier for twinning is proportional to the change of surface energy associated with the twinning. Thus, the transition of deformation modes can be attributed to the change of surface energy as a function of the cross-sectional shape.

**KEYWORDS:** dislocation slip, twinning, plasticity, nanowire, in situ TEM

etallic nanowires (NWs) have been widely used in a variety of nanoengineering applications, including nanoelectromechanical systems, nanosensors, transparent electrodes, optoelectronics, and flexible and stretchable electronics.<sup>1-5</sup> Mechanical behaviors of metallic NWs play a crucial role in reliability of the NW-based devices. Different from bulk materials, surface dislocation nucleation has been identified as a dominant deformation mechanism in NWs. Extensive research has been performed on defect-free, singlecrystalline metallic NWs where surface-nucleated dislocations tend to slip across the NW, $^{6-17}$  as a result of two competitive deformation mechanisms, twinning and localized dislocation slip. 18,19 The former leads to large plasticity, while the latter results in limited plasticity. Thus, it is of interest to study how the two deformation mechanisms compete with each other in face-centered cubic (FCC) metallic NWs and what the underlying factors are.

The size effect of nanomaterials not only affects the material strength but also changes the corresponding deformation mechanism. 6,13,20-23 Transition from slip to deformation twinning in FCC metals has been observed with the grain size or wire diameter close to the nanoscale. 13,24,25 Twinning deformation accompanied by large plasticity has been reported in single-crystalline FCC metallic NWs. 25-27 However, localized dislocation slip has also been observed, leading to limited plastic deformation. 22,28,29 It has been recently reported that the deformation mechanisms could be affected by preexisting internal structures<sup>29-31</sup> (e.g., twinning boundary). Deformation twinning and dislocation slip are in direct competition since both occur through dislocation processes operating on the same set of slip systems.<sup>8,21</sup> However, comprehensive understanding of what factors affect the deformation modes in single-crystalline FCC NWs is still lacking.

Here, based on in situ tensile tests using transmission electron microscopy (TEM) and molecular dynamics (MD) simulations, we report that the cross-sectional shape is an additional factor that can affect the competition between

Received: April 29, 2019 Accepted: July 15, 2019 Published: July 15, 2019



<sup>&</sup>lt;sup>†</sup>School of Engineering, Brown University, Providence, Rhode Island 02912, United States

<sup>\*</sup>Department of Mechanical and Aerospace Engineering, North Carolina State University, Raleigh, North Carolina 27695, United States

<sup>§</sup>Department of Materials Science and Engineering, University of California, Berkeley, California 94720, United States

Max Planck Institute for Intelligent Systems, Heisenbergstrasse 3, D-70589 Stuttgart, Germany

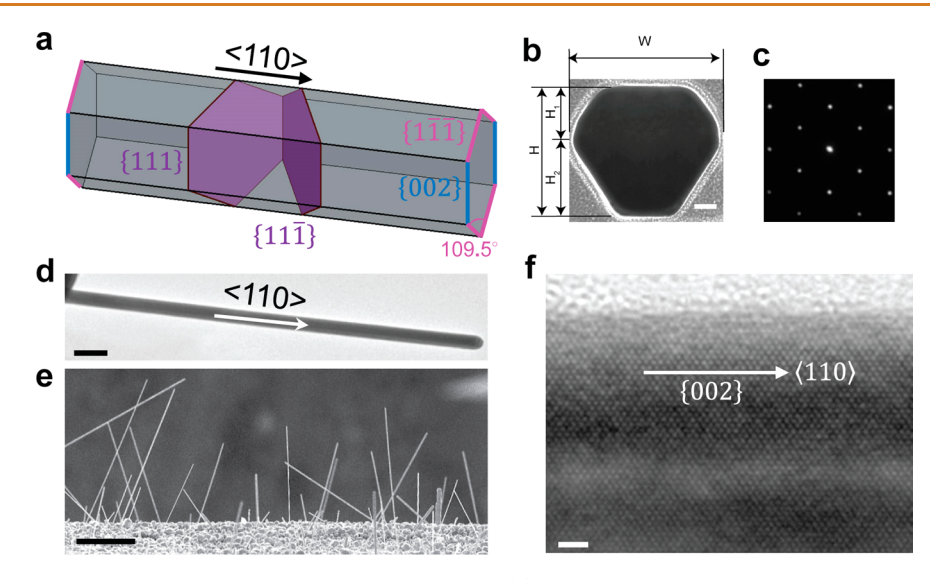


Figure 1. Microstructure characterization of single-crystalline Ag NWs. (a) Schematic drawings of single-crystalline structure with length direction along  $\langle 110 \rangle$  direction. (b, c) Cross-sectional TEM image and a corresponding diffraction pattern of a single-crystalline Ag NW. The cross-sectional geometry of the NW is described by parameters W,  $H_1$ , and  $H_2$ . Scale bar: 20 nm. (d) TEM image of a single-crystalline Ag NW with a growth direction of  $\langle 110 \rangle$ . Scale bar: 100 nm. (e) Scanning electron microscope image of crystalline Ag NWs synthesized by physical vapor deposition. Scale bar: 5 um. (f) High-resolution TEM image showing the crystallinity of the single-crystalline Ag NW in (d). Scale bar: 2 nm.

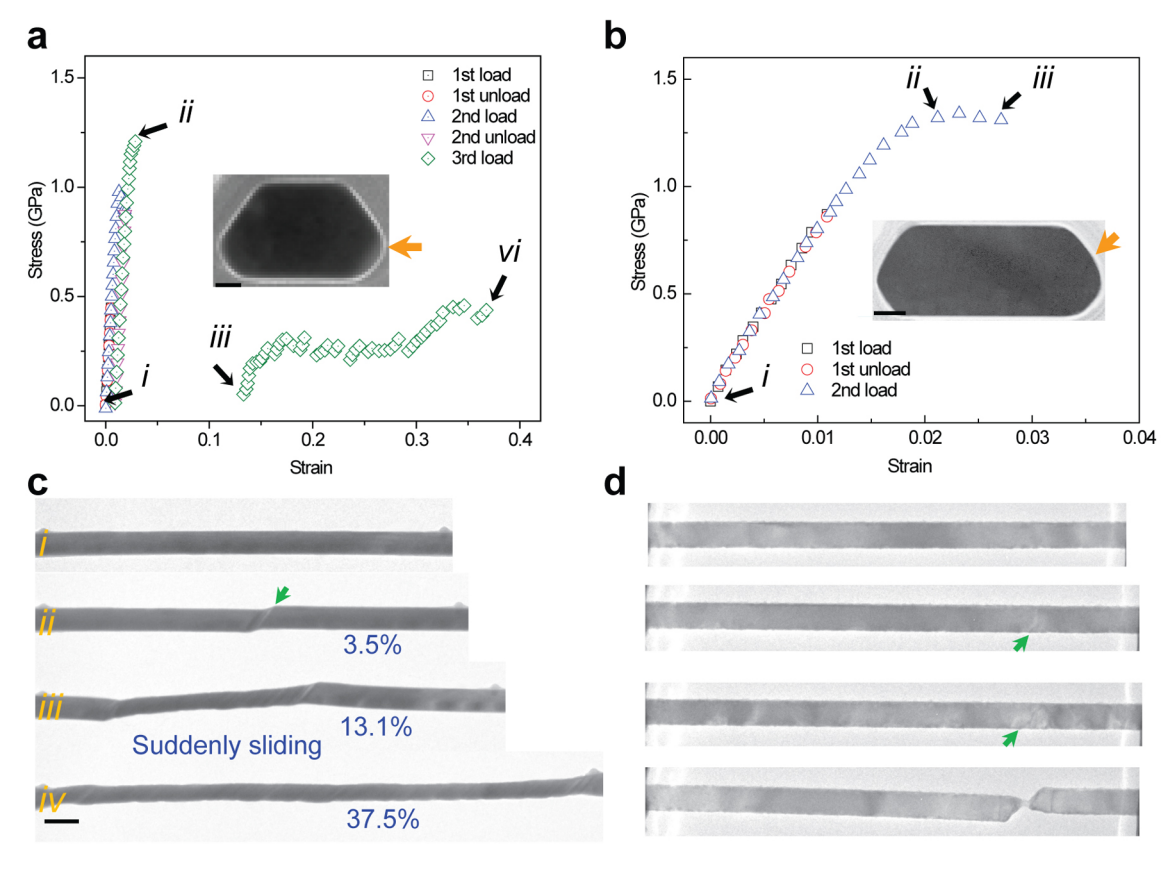


Figure 2. Mechanical behaviors and microstructure evolutions of single-crystalline Ag NWs under in situ TEM tensile tests. (a, b) Engineering stress-strain curves of two single-crystalline Ag NWs with different aspect ratios. Insets in (a) and (b) are the corresponding cross-sectional images of the tested NWs (sectioned from the undeformed part after the test). Scale bar: 20 nm. (c, d) Snapshots of microstructure evolutions corresponding to (a) and (b). The four snapshots in each case correspond to the stresses and strains marked in (a) and (b). Planar sliding is labeled by green arrows. Scale bars: 100 nm. The viewing directions in (a) and (b), marked by the yellow arrows in the insets, are from the  $\langle 1\bar{1}0 \rangle$  and  $\langle 111 \rangle$  zone axes, respectively.

deformation mechanisms in single-crystalline FCC metallic NWs. For a truncated rhombic cross-section, the extent of

truncation determines the competition. Specifically, a transition from twinning to localized dislocation slip occurs with

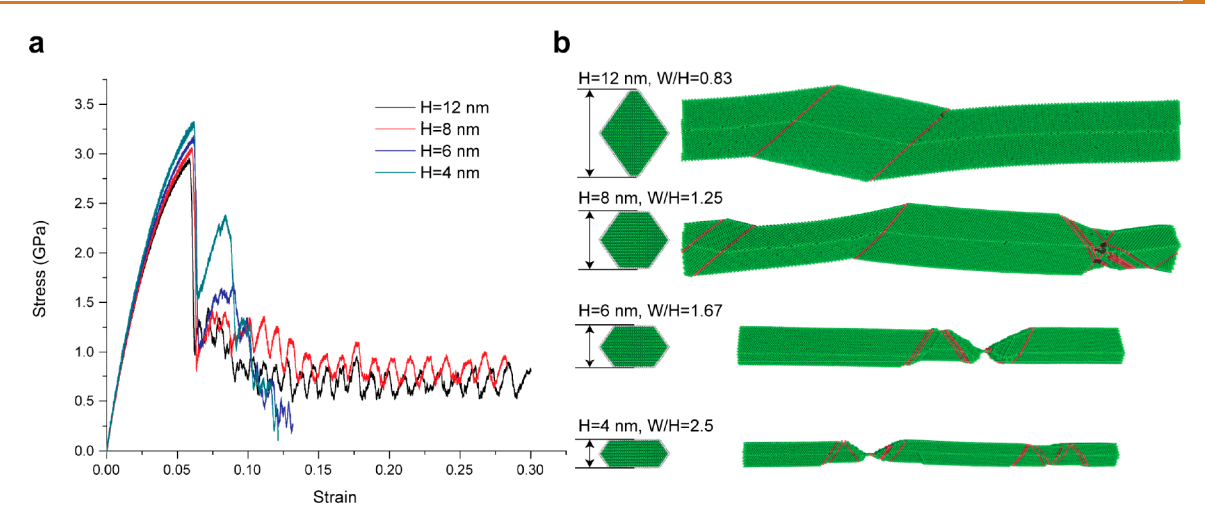


Figure 3. Tensile deformation of single-crystalline Ag NWs with different cross-sectional geometries and calculation of energy barriers of twinning and slip fault. (a) Stress-strain curves of four representative cases. (b) Cross-sectional geometries and deformation modes. Twinning deformation is dominating in cases where H = 12 and 8 nm. Slip failures are observed in cases where H = 6 and 4 nm.

increasing extent of truncation (or increasing aspect ratio). Theoretical and simulation results indicate that the energy barriers for twinning and dislocation slip depend on the cross-sectional shape of the NW. The energy barrier for twinning is proportional to the change of surface energy associated with the twinning, and we conclude that the transition of deformation modes can be attributed to the change of surface energy as a function of the cross-sectional shape.

# **RESULTS AND DISCUSSIONS**

NW Morphology and in Situ TEM Tensile Testing. Microstructure characterization of single-crystalline Ag NWs is shown in Figure 1. Figure 1a shows schematically the geometry of the single-crystalline NW in which some important crystal planes and surface facets are labeled. The single-crystalline NWs exhibit a truncated rhombic cross-section (see a typical example in Figure 1b). To quantify the cross-sectional shape, the thickness and width are defined as the edge-to-edge length perpendicular and parallel to the {002} surface, respectively, as shown in Figure 1b. It should be noted that the singlecrystalline Ag NWs exhibited high crystalline quality owing to near-equilibrium growth conditions via physical vapor deposition. The NWs are straight and uniform in crosssectional shape, with the growth direction of (110) (Figure 1d,e). As shown in the high-resolution TEM image in Figure 1f, the NW shows a perfect atomic structure along the longitudinal direction and a uniform atomic arrangement at {002} surface facets.

In situ TEM tensile testing of NWs was performed on a microelectromechanical system (MEMS)-based tensile testing stage (see Supplementary Figure 1). The load and displacement can be accurately measured using this MEMS device, along with concurrent, real-time imaging of microstructure evolution during deformation. In Figure 2, we show stress—strain curves and snapshots of microstructure changes for tensile tests of two single-crystalline Ag NWs. Insets in Figures 2a,b are the corresponding cross-sectional TEM images of the tested NWs, taken from the undeformed part (beyond the clamps). The two NW cross-sections, as shown in the insets of Figure 2a,b, possess different levels of truncation or, more quantitatively, different aspect ratios of 1.67 and 2.51 (defined as W/H), respectively.

The two single-crystalline NWs showed different plastic behaviors, as shown in Figure 2. The one in Figure 2a,c with small aspect ratio (W/H) showed large plasticity, *i.e.*, an elongation of 37.5% for the fully deformed part between the two local markers (Figure 2c-iv), while the other with a large aspect ratio in Figure 2b,d displayed limited plasticity. Moreover, the yield strength and the ultimate tensile strength (UTS) of the two tested NWs were found to be 0.95 and 1.21 GPa and 1.15 and 1.34 GPa, respectively.

Transition of Deformation Modes. In situ tensile testing of the single-crystalline Ag NW with a relatively small aspect ratio in Figure 2a,c revealed large plasticity as a result of deformation twinning. The microstructure evolution in the single-crystalline Ag NW during the plastic deformation is illustrated in Figure 2c (also see Supplementary Movie 1). At the yielding point, leading partials were nucleated from the NW free surface and propagated across the entire crosssection, which resulted in a permanent planar slip (a segment of nanotwins) (Figure 2c-ii). Nucleation and propagation of the leading partials continued; followed by a sudden, large elongation of the NW accompanied by a nearly full release of the applied stress (Figure 2c-iii). After that, the NW underwent a continuous twinning deformation, leading to large plastic deformation and accompanied by an increase of the applied load (Figure 2c-iv).

In contrast to the deformation twinning, localized dislocation slip dominates in the single crystalline NW with the relatively large aspect ratio, leading to limited plasticity, as shown in Figure 2b,d. As the applied stress exceeded the yielding point, dislocations nucleated from the free surface and propagated into the NW (Figure 2d-ii,iii). Further loading caused continuous dislocation nucleation and propagation at the same position and sudden failure of the NW (Figure 2d-iv).

The above results suggested that there is a transition of deformation mechanisms from twinning to dislocation slip with increasing extent of truncation. A similar transition has been found by MD simulations;<sup>35,36</sup> however, our work is a systematic experimental study of FCC metallic NWs with different cross-sectional geometries. The transition was confirmed by more experimental and simulations results (see Supplementary Figure 2 and Figure 5c). Morphology control

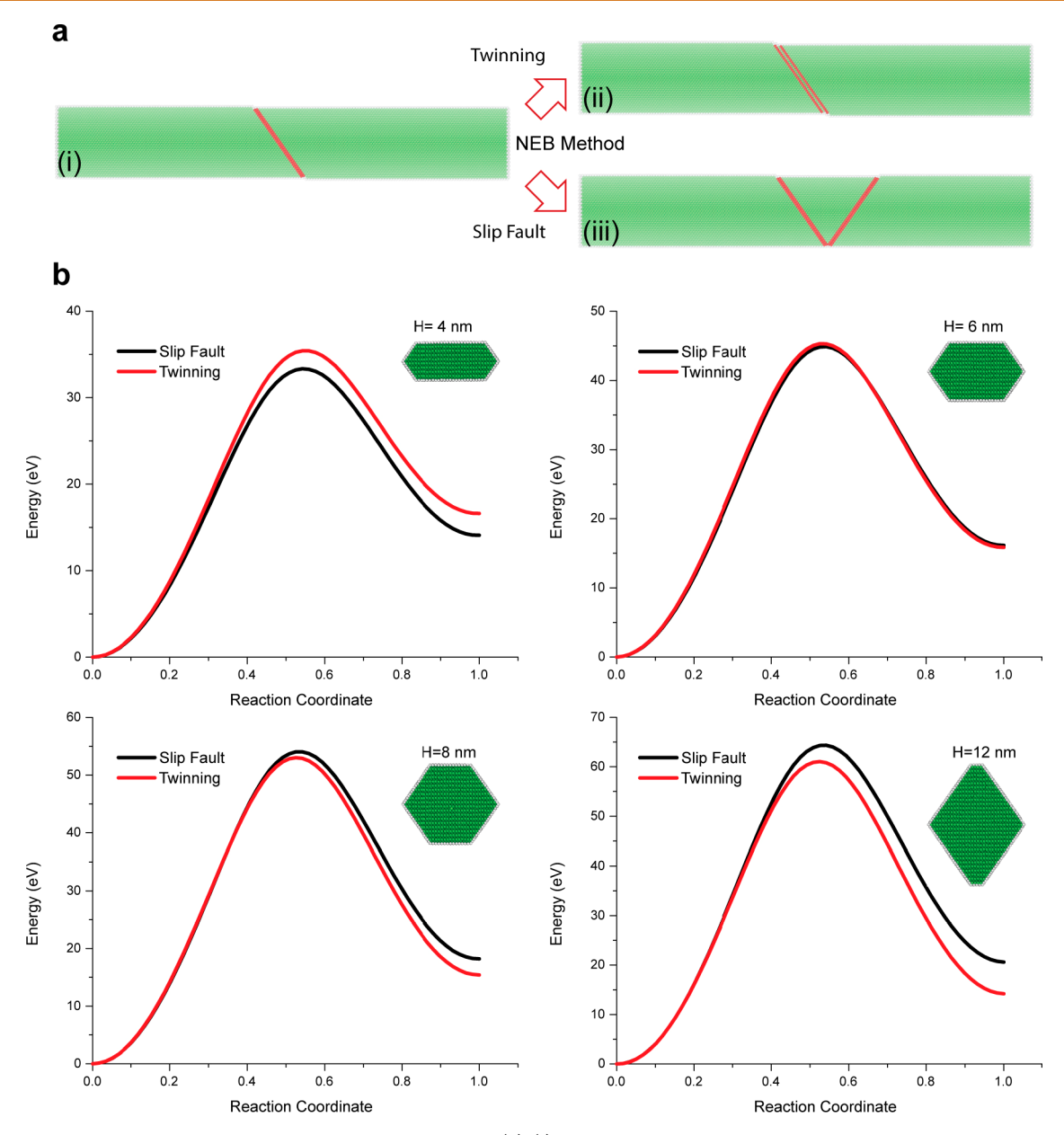


Figure 4. Calculation of energy barriers of twinning and slip fault. (a) (i) Initial configuration of NEB calculation with one intrinsic SF in the NW. (ii) Twinning configuration. (iii) Slip fault configuration. (b) Energy barriers of twinning and slip fault calculated by NEB for four different cross-sectional geometries.

of NWs and other nanostructures is an important goal in the synthesis of nanomaterials.<sup>37,38</sup> In general, the cross-sectional shape follows the Wulff construction, where the facets correspond to low-free-energy planes such as {111} and {001}. For example, Si nanowires with a  $\langle 110 \rangle$  axial direction synthesized by a very different method, chemical vapor deposition (CVD), exhibit the identical cross-sectional shape (*i.e.*, truncated rhombus with four {111} and two {001} facets).<sup>39</sup>

To reveal the underlying mechanisms responsible for the observed transition of deformation modes in single-crystalline  $\langle 110 \rangle$ -oriented Ag NWs, a series of MD simulations were carried out. Single-crystalline Ag NWs with four representative aspect ratios (with different thickness H but a fixed width W) were first simulated. Figure 3a shows the stress—strain curves of the four cases, and Figure 3b shows the cross-sectional geometries and corresponding deformation modes under

tensile loading. NWs with small aspect ratios (W = 10 nm, H = 12 or 8 nm) underwent large plastic strain through twinning deformation (also see Supplementary Movie 2). A leading partial was initially nucleated at the corner of two {111} surfaces and propagated through the NW, leaving a stacking fault behind in the NW. Continuous twinning partials were further nucleated on the stacking fault, leading to twin migration and reorientation of the NW upon further loading. As the aspect ratio increased (W fixed while the H value decreases), the NWs failed by slip with limited plastic strain. Same as the twinning case, the leading partial was nucleated at the corner of two {111} surfaces, leaving a stacking fault in the NW. However, instead of twinning partials nucleated on the stacking fault, a new leading partial was nucleated from the surface step on the inclined slip plane, on the opposite side from where the first leading partial was nucleated. This created a new intrinsic stacking fault, which formed a V shape with the

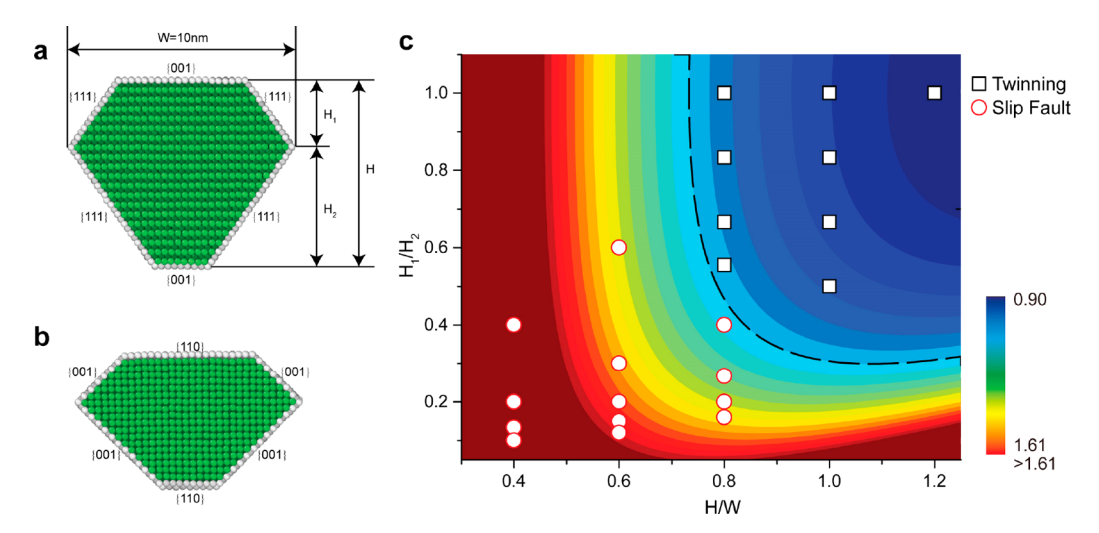


Figure 5. Effect of cross-sectional geometry in MD simulations. (a) Cross-sectional geometry of a typical  $\langle 110 \rangle$  single-crystalline NW. (b) Cross-sectional geometry of reoriented  $\langle 001 \rangle$  NW from (a) with  $\{001\}$  and  $\{111\}$  facets reoriented to  $\{110\}$  and  $\{001\}$  facets. (c) Contour plot of normalized surface energy change as a function of H/W and  $H_1/H_2$  along with the observed deformation modes from simulation. Open black squares stand for the twinning-dominated mode, and open red circles stand for the slip-dominated mode.

previous stacking fault, as shown in Figure 4a-iii. More leading partials may be nucleated and form multiple V-shaped regions along the NW. Similar zigzag stacking faults have been observed in Al NWs recently, also showing limited plasticity. Under further loading, trailing partials and twinning partials were nucleated in one of the V-shaped regions, leading to localized necking, and the NW eventually failed with limited plastic strain (also see Supplementary Movie 3). The simulation results are consistent with our *in situ* experimental observations and previous MD simulations. <sup>21,35,41</sup>

Extensive studies have been reported to predict the plastic deformation mechanisms in FCC metallic NWs. The deformation mechanisms were found to be strongly dependent on the axial orientation, loading type, stacking fault energy, and cross-sectional geometry. The large plasticity in tensile tests of (110)-oriented NWs by deformation twinning has been observed in MD simulations; deformation twinning was found to result in pseudoelastic and shape-memory behaviors. <sup>21,29,41–43</sup> According to previous research on the generalized stacking fault (GSF) energy <sup>44,45</sup> and twinning energy curves, the intrinsic SF, unstable SF, and unstable twinning energies were identified as the most important intrinsic parameters that play key roles in the plasticity of FCC metal NWs. A twinnability parameter 19 based on these parameters has been defined to predict the plasticity mechanisms in FCC bulk metals. Weinberger and Cai's twoparameter criterion<sup>8</sup> based on both the Schmid factor and GSF can predict the plastic deformation mechanism in FCC metal NWs under uniaxial loading. The effect of the cross-sectional shape was considered in a surface SF energy approach by Jiang et al. 46 to predict the surface-nucleated plasticity in FCC metal NWs. Surface energy was found to play an important role in deformation of Au NWs.<sup>26</sup>

Similar to the surface SF energy approach,  $^{46}$  in this work we applied the nudged-elastic-band (NEB) method  $^{47}$  to calculate the energy barriers of twinning ( $E_{\rm ut}$ ) and slip fault ( $E_{\rm sf}$ ) to predict the transition of deformation mechanisms in single-crystalline  $\langle 110 \rangle$ -oriented Ag NWs. The NEB method is more accurate in calculating the energy barriers than the more conventional approach of rigidly shifting the atoms along a slip plane  $^{46}$  when free surfaces and different cross-sectional

geometries are included. Combined with the *in situ* TEM experimental results, we systematically studied the effects of cross-sectional geometry on the deformation behaviors of single-crystalline metal NWs and identified the correlation between the energy barriers and the surface energy change.

It is well known that surface dislocation nucleation is typically the dominating deformation mechanism for the onset of plasticity in an NW.  $^{11}$  An intrinsic SF is introduced into the NW by shearing a {111} plane along the (112) direction, as shown in Figure 4a-i, which after relaxation serves as the initial configuration for energy barrier calculation. Twinning and slip fault are possible succeeding deformation pathways after the nucleation of the intrinsic SF. To construct the twinning configuration, a neighboring {111} plane of the intrinsic SF is sheared in the same (112) direction and relaxed, as shown in Figure 4a-ii. This is the final configuration for energy barrier calculation of twinning. For the slip fault configuration, a second intrinsic SF is introduced similar to the first one but in another {111} plane, as shown in Figure 4a-iii. Since the nucleation of a second slip fault is energetically more favorable than direct nucleation of an intrinsic SF in a perfect lattice, the atomic configuration in Figure 4a-iii is used as the final configuration for energy barrier calculation of the slip fault.

The competition of twinning and slip can be determined by a simple criterion: which of the two energy barriers, barrier of twinning  $E_{\rm ut}$  or barrier of slip fault  $E_{\rm sf}$  is larger? When  $E_{\rm ut}$  is lower than  $E_{\rm sf}$  the twinning deformation is energetically more favorable; otherwise slip is more favorable. The NEB method was adopted to calculate the barriers of twinning and slip for the four representative NWs shown in Figure 4. When H is 4 or 6 nm,  $E_{\rm sf}$  (black line) is smaller than  $E_{\rm ut}$  (red line), and the NWs fail by slip, as found by the MD simulations in Figure 3b. With increasing H, the difference of twinning barrier and slip fault barrier becomes smaller. When H reaches 8 or 12 nm,  $E_{\rm ut}$ becomes smaller than  $E_{sb}$  and as a result, the deformation mechanism transits from slip to twinning, consistent with the MD simulations (Figure 3b). By comparing the energy barriers of twinning and slip fault, the deformation mechanisms in single-crystalline (110) NWs can thus be predicted.

To systematically investigate the effects of cross-sectional geometry on the transition of deformation mechanisms in

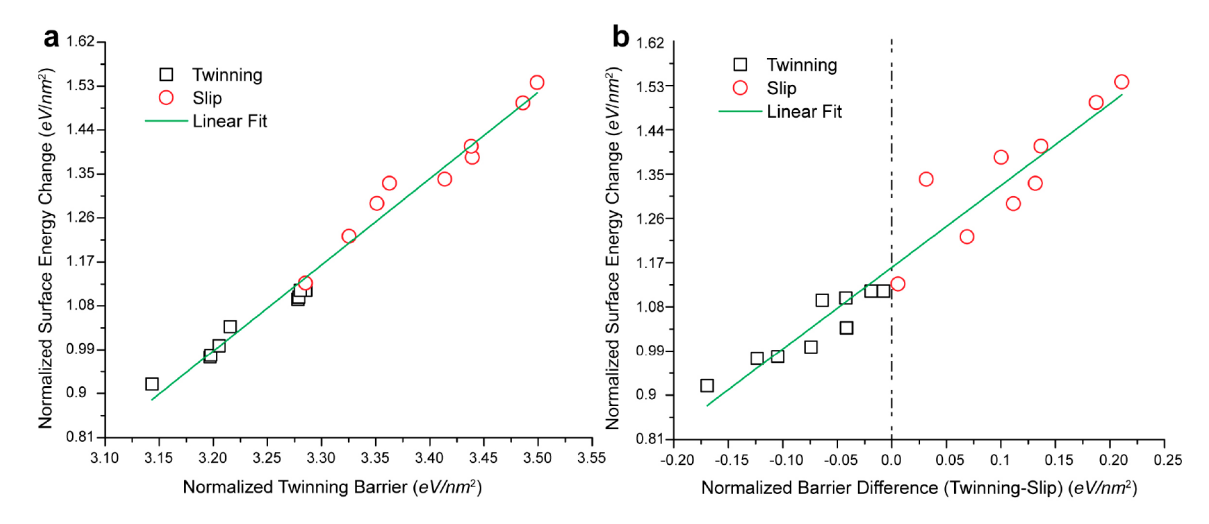


Figure 6. (a) Normalized twinning energy barrier is linearly correlated to the surface energy change. (b) Normalized barrier difference between twinning and slip fault is linearly correlated to the surface energy change, which can predict the deformation mode in a (110) single-crystalline NW. The black squares stand for twinning deformation, and the red circles for slip deformation in MD simulations.

single-crystalline metallic NWs, a parametric study was conducted in MD simulations. Figure 5a shows the crosssectional geometry of the simulated NWs, similar to those used in our experiments, where W, H, and  $H_1$  are the independent geometric parameters. NEB calculations were conducted to determine the energy barriers for twinning and slip fault similar to Figure 4, and tensile tests were performed on the samples until failure to identify the actual deformation mode. Details of the simulations can be seen in Methods. For a constant W = 10nm, the energy barriers of twinning  $(E_{ut})$  and slip fault  $(E_{sf})$  for different values of H and  $H_1$  are calculated. To evaluate the effect of the cross-sectional geometry, the barriers of twinning and slip fault are all normalized by the cross-sectional area as shown in Supplementary Table 1. For the twinning deformation, twinning partials lead to reorientation of the (110)-oriented NWs to become (001)-oriented, as shown in Figure 5a,b, where the original {111} and {001} side surfaces in Figure 5a are reoriented to {001} and {110} in Figure 5b. In FCC metals {111} planes have the lowest surface energy, followed by {100} and then {110} planes. 48 Thus, the surface energy of the NW should increase after the twinning deformation. When calculating the increment of surface energy of (110) NW due to twinning, we consider a unit length in the axial direction; after twinning, this length in the new (001) axial direction will become  $\sqrt{2}$  times the initial length. The increase of the surface energy due to twinning can be formulated as a function of cross-section geometry:

$$\begin{split} \Delta E &= \tilde{S}_{110} \gamma_{110} + \tilde{S}_{001} \gamma_{001} - S_{001} \gamma_{001} - S_{111} \gamma_{111} \\ &= \sqrt{2 \tilde{l}_{110} \gamma_{110}} + \sqrt{2 \tilde{l}_{001} \gamma_{001}} - l_{001} \gamma_{001} - l_{111} \gamma_{111} \\ &= \sqrt{2 \gamma_{110} \gamma_{110}} l_{001} + (1.218 \gamma_{110} - \gamma_{111}) l_{111} \end{split} \tag{1}$$

where  $\Delta E$  is the surface energy change per unit axial length in twinning deformation,  $\tilde{l}_{110} = l_{001}\tilde{l}_{001} = 0.8615l_{111}$ , S and l are area and total length of the cross-section in a specific orientation before reorientation as shown in Figure 5a, respectively, and  $\tilde{S}$  and  $\tilde{l}$  are corresponding parameters after reorientation as shown in Figure 5b.  $\Delta E$  is normalized by the cross-sectional area:

$$\Delta E(W, H_1, H_2) = \frac{(\sqrt{2}\gamma_{110} - \gamma_{001})l_{001} + (1.218\gamma_{001} - \gamma_{111})l_{111}}{S_{cross}} = [(\sqrt{2}\gamma_{110} - \gamma_{001})l_{001} + (1.218\gamma_{001} - \gamma_{111})l_{111}] / WH - \frac{H_1^2 + H_2^2}{\sqrt{2}}$$
(2)

Note that in addition to obtaining the energy barriers for slip and twinning from NEB, the values of the twinning energy curve at reaction coordinate = 1 in Figure 4b are essentially the same as the surface energy change induced by twinning as calculated using eq 2. For a comparison of the NEB simulation results with eq 2, see Supplementary Figure 3.

The values of normalized twinning barrier  $\hat{E}_{\mathrm{ut}}$  and slip fault barrier  $\hat{E}_{\rm sf}$  are shown in Supplementary Table 1, which depend on the cross-sectional geometry. When the barrier difference  $(E_{\rm ut} - E_{\rm sf})$  changes from negative to positive, the deformation mode transits from twinning to slip, as expected. In Supplementary Table 1, the normalized surface energy change  $\Delta \tilde{E}$  for each case also depends on the cross-sectional geometry based on eq 2. Figure 5c shows the contour of  $\Delta E$  with a constant value of W = 10 nm. The x-axis of the contour is H/W, and the y-axis is  $H_1/H_2$ . The transition from blue to red color in the contour indicates an increase in  $\Delta \hat{E}$ . Although the absolute value of  $\Delta \hat{E}$  depends on W, the contour lines remain the same regardless of W. Similar to Figure 3, the deformation modes of all the NWs were determined by the MD simulations and plotted in Figure 5c. Black squares stand for the twinningdominated mode, and red circles stand for the slip faultdominated mode. According to the color contour and the simulation data points in Figure 5c, it is found that the deformation modes can also be determined by the value of  $\Delta E$ in addition to the energy barrier difference. The dashed contour line in Figure 5c represents the critical value of  $\Delta \hat{E}$  for the deformation modes' transition in the NWs. Besides W = 10nm, NWs with W = 15 nm were also calculated, which shows the same results as W = 10 nm, indicating that the results are only dependent on H/W and  $H_1/H_2$ , but not the NW size in this range (see Supplementary Figure 4).

With gliding of each twinning partial, a unit layer of a (110) lattice is reoriented to a (001) lattice and the free surface energy increment is induced in the twinning region. In the twinned region of an NW, even with only one twinning partial, the original {111} surface is reoriented to the {001} surface and the original {001} surface is reoriented to the {110} surface (Figure 5b). As a consequence, from an energy point of view, the most significant change of the whole system after twinning is the free surface energy increment, which is of critical importance for the plasticity of NWs. The surface energy increment associated with twinning deformation in the twinned region is a result of the accumulation of gliding twinning partials. Hence this surface energy change, which can be written as a function of cross-sectional geometry parameters, is expected to be linearly correlated with the twinning partial-induced energy change in the NW, and there should also be a correlation between this surface energy change and the twinning energy barrier. Figure 6a plots the normalized twinning energy barrier versus the normalized surface energy change. Our NEB simulation data in Supplementary Table 1 clearly show that the twinning energy barrier is linearly correlated to the surface energy change. For the slip fault deformation, which is not associated with lattice reorientation but only atomic steps on the free surface, the energy barrier is relatively constant for different cross-sectional geometries, as compared to the twinning energy barrier. Figure 6b shows the difference of twinning energy barrier and slip fault barrier ( $E_{ut}$  $-\hat{E}_{\rm sf}$ ) versus the surface energy change. This barrier difference is also linearly correlated to the surface energy change. The discovery of this linear correlation of the energy barrier difference with the surface energy change can predict the deformation mode in NWs more easily. In summary, by comparing the energy barriers of twinning and slip fault, the deformation mechanism in single-crystalline Ag (110) NWs with different cross-sectional geometries can be predicted. A key determining factor of deformation mechanism seems to be the surface energy change due to twinning partial-induced lattice reorientation, which is found to be linearly correlated to the difference in energy barriers associated with twinning and

Can this method summarized above be generalized to other low stacking fault FCC metals? We applied this approach to two other low stacking fault FCC metals: Cu and Au. Supplementary Figure 5a,c plot the normalized twinning energy barrier versus the normalized surface energy change in Cu and Au, respectively, which show perfectly linear correlation between the twinning energy barrier and the surface energy change. The barrier difference is also linearly correlated to the surface energy change in Cu and Au, as shown in Supplementary Figure 5b,d, respectively. The deformation modes in tensile tests in single-crystalline Cu and Au (110) NWs can be predicted by this method. The critical surface energy change  $\Delta \hat{E}$  for the deformation mechanism transition can be different for different materials. In the current model, the critical  $\Delta \hat{E}$  values for Ag, Cu, and Au are 1.12, 1.84, and 1.86 eV/nm<sup>2</sup>, respectively. These results imply that the surface energy change also plays a critical role in the deformation mechanism of NWs in additional to dislocations; such a surface energy criterion may also be applied to other FCC metals and possibly even some of the BCC NWs.

Although the simulation results are self-consistent, some caution is called for when seeking quantitative comparisons

with experiments, as the deformation modes predicted from MD can depend on the accuracy of the adopted interatomic potentials. Temperature, loading rate, and initial defects in experimental samples may also introduce some stochastic events and affect the results. In our NEB approach, the energy barriers were calculated at zero temperature; however, the simulations of tensile tests were conducted at finite temperature. Thermal fluctuation can introduce some stochastic effect in deformation mode when the tensile simulations were at a temperature of 300 K or higher, especially for the cases with a small barrier difference.

## **CONCLUSIONS**

We have systematically studied the transition between two deformation mechanisms, twinning and dislocation slip, in single-crystalline FCC metallic Ag NWs using combined in situ TEM tensile testing, microstructure characterization, and MD simulations. Twinning deformation accompanied by large plasticity was identified in the NWs with small aspect ratios. A transition of deformation modes from twinning to dislocation slip was observed as the aspect ratio increased. Specifically, as the cross-sectional shape changed from regular hexagonal shape to ribbon-like hexagonal shape, a transition from twinning to dislocation slip occurred. Using MD simulations, we systematically studied the effects of crosssectional geometry on the deformation behavior of singlecrystalline metal NWs. Through the NEB calculation of energy barriers of twinning and slip fault in NWs with different crosssectional geometries, we can predict the deformation mechanisms in single-crystalline Ag (110) NWs. A key determining factor of deformation mechanism was shown to be the surface energy change due to twinning partial-induced lattice reorientation, which was found to be linearly correlated to the difference in energy barriers associated with twinning and slip. The critical  $\Delta E$  (normalized surface energy change) for Ag, Cu, and Au was found to be 1.12, 1.84, and 1.86 eV/ nm<sup>2</sup>, respectively. This method was successfully applied to other low stacking fault energy FCC metals, such as Cu and Au NWs.

# **METHODS**

Sample Synthesis and Characterization. Crystalline Ag NWs were synthesized by physical vapor deposition inside a molecular beam epitaxy system under ultra-high-vacuum conditions and a substrate temperature of 700  $^{\circ}$ C. More details of the NW synthesis process are provided elsewhere. <sup>28</sup>

Cross-sectional TEM samples of Ag NWs before and after deformation were prepared with focused ion beam. High-resolution TEM observations were performed on JEOL 2010F with a Schottky field emission gun (FEG) operated at 200 kV and a probe-corrected FEI Titan  $\rm G^2$  60–300 kV S/TEM equipped with an X-FEG source operated at 200 kV.

In Situ SEM/TEM Mechanical Testing. The mechanical testing was carried out *in situ* inside a TEM using a MEMS-based material testing stage, which consists of an electrostatic (comb-drive) actuator, a capacitive load sensor, and a gap in between for mounting samples. Details on the testing stage have been reported previously. <sup>32,33</sup> Displacement (and strain) is measured by digital image correlation of TEM images of two local markers on the specimen. This MEMS-based testing stage has a strain resolution of 0.01% (gage length 2  $\mu$ m) and a stress resolution of 1.4 MPa (for example, for an NW diameter of 104 nm<sup>31</sup>).

NWs were mounted on the testing stage using a nanomanipulator (Klocke Nanotechnik, Germany) inside a FEI Nova 600 dual beam. A single Ag NW was welded to the nanomanipulator probe, then

mounted to the MEMS stage and clamped by electron-beam-induced Pt deposition at the two free ends. Two local markers were deposited on the NWs for displacement (and strain) measurement. *In situ* TEM mechanical testing was performed on a JEOL 2010F operated at 200 kV. The loading and unloading strain rates were ~0.003%/s. Low-magnification images were recorded at a fixed condenser (the second condenser lens) current to minimize the focus change. The current density of the incident e-beam is <0.1 A/cm², and its effect on the mechanical behavior of the NW under tensile testing can be neglected.

MD Simulations. Large-scale MD simulations were performed using the software package LAMMPS. 49 Figure 5a shows the atomic cross-section of the single-crystalline NW samples. For each sample, W equals 10 nm and H ranges from 4 to 13.5 nm, and all samples are 80 nm in length. The embedded atom method potential for Ag, 5 Cu,<sup>51</sup> and Au<sup>52</sup> was used to describe the interatomic interactions. Periodic boundary conditions were imposed along the axial direction (that is, the loading direction (110)) of all simulated samples. The samples were initially relaxed and equilibrated at a temperature of 10 K for 800 ps using a Nosé-Hoover<sup>53</sup> thermostat and barostat, followed by stretching at a constant strain rate of 108 s<sup>-1</sup> under NVT ensemble (canonical ensemble) until failure. The NEB method used the NEB modulus of LAMMPS.<sup>49</sup> To visualize defects generated during deformation, atoms were painted with different crystalline order in different colors using a common neighbor analysis by OVITO.<sup>54</sup> The green-colored atoms stand for atoms with facecentered cubic symmetry, the red ones those with hexagonal closepacked symmetry, and the gray ones those at dislocation cores, surfaces, and point defects. The surface energies used in eq 2 are calculated from Mishin's EAM potential so with values of  $\gamma_{111} = 0.86 \, \text{J/}$  $m^2$ ,  $\gamma_{001} = 0.94 \text{ J/m}^2$ , and  $\gamma_{110} = 1.01 \text{ J/m}^2$ .

#### **ASSOCIATED CONTENT**

## **S** Supporting Information

The Supporting Information is available free of charge on the ACS Publications website at DOI: 10.1021/acsnano.9b03311.

Detailed notes of additional information on *in situ* TEM tensile tests and more *in situ* TEM tensile tests of single-crystalline Ag NWs; normalized surface energy difference from a closed form solution and NEB simulations; more MD simulation tests of single-crystalline Ag NWs with W=15 nm; prediction of energy barrier approach for Cu and Au  $\langle 110 \rangle$ -oriented NWs (PDF)

Supporting movie (MP4) Supporting movie (AVI) Supporting movie (AVI)

#### **AUTHOR INFORMATION**

# **Corresponding Authors**

\*E-mail: huajian\_gao@brown.edu. \*E-mail: yong\_zhu@ncsu.edu.

ORCID ®

Sheng Yin: 0000-0001-8705-9950 Yong Zhu: 0000-0002-3862-5757

# **Author Contributions**

 $^{\perp}$ S.Y. and G.C. contributed equally to this work.

#### **Notes**

The authors declare no competing financial interest.

# **ACKNOWLEDGMENTS**

G.C. and Y.Z. acknowledge financial support from the National Science Foundation (NSF) under Award No. DMR-1410475. S.Y. and H.G. acknowledge financial support from the NSF through Grant DMR-1709318 and computational support by

the Extreme Science and Engineering Discovery Environment (XSEDE) through Grant MS090046. We are grateful to Dr. Xiahan Sang (Oak Ridge National Lab.) for MATLAB codes for image processing. The authors acknowledge the use of the Analytical Instrumentation Facility (AIF) at North Carolina State University, which is supported by the State of North Carolina and the National Science Foundation (award number ECCS-1542015). The AIF is a member of the North Carolina Research Triangle Nanotechnology Network (RTNN), a site in the National Nanotechnology Coordinated Infrastructure (NNCI).

## **REFERENCES**

- (1) Lee, J.-Y.; Connor, S. T.; Cui, Y.; Peumans, P. Solution-Processed Metal Nanowire Mesh Transparent Electrodes. *Nano Lett.* **2008**, *8*, 689–692.
- (2) Tao, A.; Kim, F.; Hess, C.; Goldberger, J.; He, R.; Sun, Y.; Xia, Y.; Yang, P. Langmuir—Blodgett Silver Nanowire Monolayers for Molecular Sensing Using Surface-Enhanced Raman Spectroscopy. *Nano Lett.* **2003**, *3*, 1229–1233.
- (3) Xu, F.; Zhu, Y. Highly Conductive and Stretchable Silver Nanowire Conductors. *Adv. Mater.* **2012**, *24*, 5117–5122.
- (4) Wang, W.; Yang, Q.; Fan, F.; Xu, H.; Wang, Z. L. Light Propagation in Curved Silver Nanowire Plasmonic Waveguides. *Nano Lett.* **2011**, *11*, 1603–1608.
- (5) Li, M.; Bhiladvala, R. B.; Morrow, T. J.; Sioss, J. A.; Lew, K.-K.; Redwing, J. M.; Keating, C. D.; Mayer, T. S. Bottom-Up Assembly of Large-Area Nanowire Resonator Arrays. *Nat. Nanotechnol.* **2008**, *3*, 88–92.
- (6) Greer, J. R.; De Hosson, J. T. M. Plasticity in Small-Sized Metallic Systems: Intrinsic *versus* Extrinsic Size Effect. *Prog. Mater. Sci.* **2011**, *56*, 654–724.
- (7) Zhu, T.; Li, J. Ultra-Strength Materials. *Prog. Mater. Sci.* **2010**, *55*, 710–757.
- (8) Weinberger, C. R.; Cai, W. Plasticity of Metal Nanowires. J. Mater. Chem. 2012, 22, 3277–3292.
- (9) Yu, Q.; Legros, M.; Minor, A. M. In Situ TEM Nanomechanics. MRS Bull. 2015, 40, 62-70.
- (10) Diao, J.; Gall, K.; Dunn, M. L. Surface-Stress-Induced Phase Transformation in Metal Nanowires. *Nat. Mater.* **2003**, *2*, 656–660.
- (11) Zhu, T.; Li, J.; Samanta, A.; Leach, A.; Gall, K. Temperature and Strain-Rate Dependence of Surface Dislocation Nucleation. *Phys. Rev. Lett.* **2008**, *100*, 025502.
- (12) Zheng, H.; Cao, A.; Weinberger, C. R.; Huang, J. Y.; Du, K.; Wang, J.; Ma, Y.; Xia, Y.; Mao, S. X. Discrete Plasticity in Sub-10-nm-Sized Gold Crystals. *Nat. Commun.* **2010**, *1*, 144.
- (13) Yue, Y.; Liu, P.; Deng, Q.; Ma, E.; Zhang, Z.; Han, X. Quantitative Evidence of Crossover Toward Partial Dislocation Mediated Plasticity in Copper Single Crystalline Nanowires. *Nano Lett.* **2012**, *12*, 4045–4049.
- (14) Chen, L. Y.; He, M.-r.; Shin, J.; Richter, G.; Gianola, D. S. Measuring Surface Dislocation Nucleation in Defect-Scarce Nanostructures. *Nat. Mater.* **2015**, *14*, 707–713.
- (15) Roos, B.; Kapelle, B.; Richter, G.; Volkert, C. Surface Dislocation Nucleation Controlled Deformation of Au Nanowires. *Appl. Phys. Lett.* **2014**, *105*, 201908.
- (16) Zhu, Y. Mechanics of Crystalline Nanowires: an Experimental Perspective. *Appl. Mech. Rev.* **2017**, *69*, 010802.
- (17) Weinberger, C. R.; Jennings, A. T.; Kang, K.; Greer, J. R. Atomistic Simulations and Continuum Modeling of Dislocation Nucleation and Strength in Gold Nanowires. *J. Mech. Phys. Solids* **2012**, *60*, 84–103.
- (18) Wu, B.; Heidelberg, A.; Boland, J. J. Mechanical Properties of Ultrahigh-Strength Gold Nanowires. *Nat. Mater.* **2005**, *4*, 525–529.
- (19) Tadmor, E.; Bernstein, N. A First-Principles Measure for the Twinnability of FCC Metals. *J. Mech. Phys. Solids* **2004**, *52*, 2507–2519.

(20) Chen, M.; Ma, E.; Hemker, K. J.; Sheng, H.; Wang, Y.; Cheng, X. Deformation Twinning in Nanocrystalline Aluminum. *Science* **2003**, *300*, 1275–1277.

- (21) Park, H. S.; Gall, K.; Zimmerman, J. A. Deformation of FCC Nanowires by Twinning and Slip. *J. Mech. Phys. Solids* **2006**, *54*, 1862–1881.
- (22) Sedlmayr, A.; Bitzek, E.; Gianola, D. S.; Richter, G.; Mönig, R.; Kraft, O. Existence of Two Twinning-Mediated Plastic Deformation Modes in Au Nanowhiskers. *Acta Mater.* **2012**, *60*, 3985–3993.
- (23) Zhu, Y. T.; Liao, X.; Wu, X. Deformation Twinning in Nanocrystalline Materials. *Prog. Mater. Sci.* **2012**, *57*, 1–62.
- (24) Wang, J.; Zeng, Z.; Weinberger, C. R.; Zhang, Z.; Zhu, T.; Mao, S. X. *In Situ* Atomic-Scale Observation of Twinning-Dominated Deformation in Nanoscale Body-Centred Cubic Tungsten. *Nat. Mater.* **2015**, *14*, 594–600.
- (25) Seo, J.-H.; Park, H. S.; Yoo, Y.; Seong, T.-Y.; Li, J.; Ahn, J.-P.; Kim, B.; Choi, I.-S. Origin of Size Dependency in Coherent-Twin-Propagation-Mediated Tensile Deformation of Noble Metal Nanowires. *Nano Lett.* **2013**, *13*, 5112–5116.
- (26) Hwang, B.; Kang, M.; Lee, S.; Weinberger, C. R.; Loya, P.; Lou, J.; Oh, S. H.; Kim, B.; Han, S. M. Effect of Surface Energy on Size-Dependent Deformation Twinning of Defect-Free Au Nanowires. *Nanoscale* **2015**, *7*, 15657–15664.
- (27) Seo, J.-H.; Yoo, Y.; Park, N.-Y.; Yoon, S.-W.; Lee, H.; Han, S.; Lee, S.-W.; Seong, T.-Y.; Lee, S.-C.; Lee, K.-B.; Cha, P.-R.; Park, H. S.; Kim, B.; Ahn, J.-P. Superplastic Deformation of Defect-Free Au Nanowires *via* Coherent Twin Propagation. *Nano Lett.* **2011**, *11*, 3499–3502.
- (28) Richter, G.; Hillerich, K.; Gianola, D. S.; Monig, R.; Kraft, O.; Volkert, C. A. Ultrahigh Strength Single Crystalline Nanowhiskers Grown by Physical Vapor Deposition. *Nano Lett.* **2009**, *9*, 3048–3052.
- (29) Cheng, G.; Yin, S.; Chang, T.-H.; Richter, G.; Gao, H.; Zhu, Y. Anomalous Tensile Detwinning in Twinned Nanowires. *Phys. Rev. Lett.* **2017**, *119*, 256101.
- (30) Yin, S.; Cheng, G.; Chang, T.-H.; Richter, G.; Zhu, Y.; Gao, H. Hydrogen Embrittlement in Metallic Nanowires. *Nat. Commun.* **2019**, *10*, 2004.
- (31) Qin, Q.; Yin, S.; Cheng, G.; Li, X.; Chang, T.-H.; Richter, G.; Zhu, Y.; Gao, H. Recoverable Plasticity in Penta-Twinned Metallic Nanowires Governed by Dislocation Nucleation and Retraction. *Nat. Commun.* **2015**, *6*, 5983.
- (32) Zhu, Y.; Espinosa, H. D. An Electromechanical Material Testing System for *In Situ* Electron Microscopy and Applications. *Proc. Natl. Acad. Sci. U. S. A.* **2005**, *102*, 14503–14508.
- (33) Chang, T.-H.; Zhu, Y. A Microelectromechanical System for Thermomechanical Testing of Nanostructures. *Appl. Phys. Lett.* **2013**, *103*, 263114.
- (34) Cheng, G.; Chang, T.-H.; Qin, Q.; Huang, H.; Zhu, Y. Mechanical Properties of Silicon Carbide Nanowires: Effect of Size-Dependent Defect Density. *Nano Lett.* **2014**, *14*, 754–758.
- (35) Leach, A. M.; McDowell, M.; Gall, K. Deformation of Top-Down and Bottom-Up Silver Nanowires. *Adv. Funct. Mater.* **2007**, *17*, 43–53.
- (36) Ji, C.; Park, H. S. Geometric Effects on the Inelastic Deformation of Metal Nanowires. *Appl. Phys. Lett.* **2006**, 89, 181916. (37) Burda, C.; Chen, X.; Narayanan, R.; El-Sayed, M. A. Chemistry
- and Properties of Nanocrystals of Different Shapes. Chem. Rev. 2005, 105, 1025–1102.
- Metal Nanocrystals. *Small* **2008**, *4*, 310–325. (39) Wu, Y.; Cui, Y.; Huynh, L.; Barrelet, C. J.; Bell, D. C.; Lieber, C. M. Controlled Growth and Structures of Molecular-Scale Silicon Nanowires. *Nano Lett.* **2004**, *4*, 433–436.

(38) Tao, A. R.; Habas, S.; Yang, P. Shape Control of Colloidal

- (40) Kim, S.-H.; Kim, H.-K.; Seo, J.-H.; Whang, D.-M.; Ahn, J.-P.; Lee, J.-C. Deformation Twinning of Ultrahigh Strength Aluminum Nanowire. *Acta Mater.* **2018**, *160*, 14–21.
- (41) Liang, W.; Zhou, M.; Ke, F. Shape Memory Effect in Cu Nanowires. *Nano Lett.* **2005**, *5*, 2039–2043.

(42) Liang, W.; Zhou, M. Atomistic Simulations Reveal Shape Memory of FCC Metal Nanowires. *Phys. Rev. B: Condens. Matter Mater. Phys.* **2006**, 73, 115409.

- (43) Park, H. S.; Gall, K.; Zimmerman, J. A. Shape Memory and Pseudoelasticity in Metal Nanowires. *Phys. Rev. Lett.* **2005**, *95*, 255504.
- (44) Vitek, V. Intrinsic Stacking Faults in Body-Centred Cubic Crystals. *Philos. Mag.* **1968**, *18*, 773–786.
- (45) Zimmerman, J. A.; Gao, H.; Abraham, F. F. Generalized Stacking Fault Energies for Embedded Atom FCC Metals. *Modell. Simul. Mater. Sci. Eng.* **2000**, *8*, 103.
- (46) Jiang, J.-W.; Leach, A. M.; Gall, K.; Park, H. S.; Rabczuk, T. A Surface Stacking Fault Energy Approach to Predicting Defect Nucleation in Surface-Dominated Nanostructures. *J. Mech. Phys. Solids* **2013**, *61*, 1915–1934.
- (47) Henkelman, G.; Uberuaga, B. P.; Jónsson, H. A Climbing Image Nudged Elastic Band Method for Finding Saddle Points and Minimum Energy Paths. *J. Chem. Phys.* **2000**, *113*, 9901–9904.
- (48) Galanakis, I.; Papanikolaou, N.; Dederichs, P. Applicability of the Broken-Bond Rule to the Surface Energy of the FCC Metals. *Surf. Sci.* **2002**, *511*, 1–12.
- (49) Plimpton, S. Fast Parallel Algorithms for Short-Range Molecular-Dynamics. *J. Comput. Phys.* **1995**, *117*, 1–19.
- (50) Williams, P. L.; Mishin, Y.; Hamilton, J. C. An Embedded-Atom Potential for the Cu-Ag System. *Modell. Simul. Mater. Sci. Eng.* **2006**, *14*, 817–833.
- (51) Mishin, Y.; Mehl, M.; Papaconstantopoulos, D.; Voter, A.; Kress, J. Structural stability and lattice defects in copper: *Ab Initio*, Tight-Binding, and Embedded-Atom Calculations. *Phys. Rev. B: Condens. Matter Mater. Phys.* **2001**, *63*, 224106.
- (52) Olsson, P. A. Transverse Resonant Properties of Strained Gold Nanowires. *J. Appl. Phys.* **2010**, *108*, 034318.
- (53) Nose, S. A Unified Formulation of the Constant Temperature Molecular-Dynamics Methods. *J. Chem. Phys.* **1984**, *81*, 511–519.
- (54) Stukowski, A. Visualization and Analysis of Atomistic Simulation Data with OVITO-the Open Visualization Tool. *Modell. Simul. Mater. Sci. Eng.* **2010**, *18*, 015012.